Buried Aseismic Slip and Off-Fault Deformation on the Southernmost San Andreas Fault triggered by the 2010 El Mayor Cucapah Earthquake revealed by UAVSAR

Jay Parker[1], Andrea Donnellan[1], Roger Bilham[2], Lisa Grant Ludwig[3], Jun Wang[4], Marlon Pierce[4], Nicholas Mowery[4]

[1] Jet Propulsion Laboratory, California Institute of Technology, Pasadena, CA, USA.

[2] Geological Sciences and Cooperative Institute for Research in Environmental Sciences, University of Colorado, Boulder, CO, USA.

[3] Program in Public Health, University of California, Irvine, CA, USA.

[4] Pervasive Technology Institute, Indiana University, Bloomington, IN, USA.

Corresponding author: Jay Parker (Jay.W.Parker@jpl.nasa.gov)

Key Points:

- Airborne radar interferograms map displacement in the Coachella Valley using visits before and after the El Mayor Cucapah earthquake.
- UAVSAR-determined triggered slip on southern San Andreas and Hidden Spring faults is discontinuous, erratic, and strike-dependent.
- Off-fault deformation co-locates with and extends beyond surface fault slip, due to slip at depth and distributed stress.

Abstract

We use UAVSAR interferograms to characterize fault slip, triggered by the Mw 7.2 El Mayor-Cucapah earthquake on the southernmost San Andreas Fault in the Coachella Valley providing comprehensive maps of landscape change that complement *in situ* measurements. Creepmeters and geological mapping of fault offsets on Durmid Hill recorded 4 mm and 8 mm of average triggered slip respectively on the fault, in contrast to radar views that reveal significant off-fault dextral deformation averaging 20 mm. Unlike slip in previous triggered slip events on the southernmost San Andreas fault, dextral shear in 2010 is not confined to transpressional hills in the Coachella valley. Edge detection and gradient estimation applied to the 50-m-sampled interferogram data identify the location (to 20 m) and local strike (to < 4°) of secondary surface ruptures. Transverse curve fitting applied to these local detections provides local estimates of the radar-projected dextral slip and a parameter indicating the transverse width of the slip, which we equate with the depth of subsurface shear. These estimates are partially validated by fault-transverse interferogram profiles generated using the web-based UAVSAR tool of GeoGateway, and appear consistent for radar-projected slip greater than about 5 mm. An unexpected finding is that creep and triggered slip on the San Andreas fault terminate in the shallow subsurface below a surface shear zone that resists the simple expression of aseismic fault slip. We introduce the notion of a surface locking depth above which fault slip is manifest as distributed shear, and evaluate its depth as 6-27 m.

Plain Language Summary

An aircraft-mounted imaging radar relies on a highly sensitive reflected interference pattern to form precise maps of surface changes. Images obtained from flights before and after the April 4, 2010 magnitude 7.2 El Mayor-Cucapah earthquake view the San Andreas Fault in California's Coachella Valley. Although the earthquake occurred seventy-five miles to the south of this fault, computer vision brings out complicated reshaping near and on the fault. The quiet deformation is concentrated in patches along the fault between the Mecca Hills and the Salton Sea, and matches the sense of slip expected from long-known continental plate motions surrounding this region. Slip at the fault surface are radar-measured at less than 3/4" but when compared to measurements in the broader fault zone we find that slip triggered by the distant earthquake is usually confined below a level thirty feet beneath the surface, reshaping a zone around the fault more than one hundred and eighty feet wide. This newly discovered barrier may be an interwoven network of clay lumps in the fault zone. Our finding explains why the process of slow fault slip is rarely obvious on the surface, but is usually observed as a series of discontinuous cracks following the fault.

1. Introduction

The Coachella Section of the San Andreas Fault (SAF) has accumulated considerable stress since its last major earthquake, c1700 CE (discussed below), and for the past few decades has exhibited surface creep amounting to 2-4 mm/yr. This southernmost ~70 km segment of the SAF is the least-well understood part of the plate-boundary-defining ~1100 km long SAF, with respect to hazard and the timing of the next large event (Philobosian, 2011). Other than the Creeping Section in central California, it is the only portion that has not had an earthquake described in historical archives and earthquake hazards have been entirely developed from paleoseismological data.

This southern section of the surface fault consists of six ≥12 km long segments. The fault is clearly expressed in hills that have formed in the transpressive zone where these segments strike at N48W, roughly 8° oblique to the local Pacific/North America slip vector, but is weakly expressed in intervening segments with similar length, low elevation and more northerly strike. Intriguingly, localized fault creep and triggered slip are almost exclusively confined to the Indio Hills, Mecca Hills and Durmid Hill segments of the fault (Bilham and Williams, 1985, Lindsey et al., 2010). Triggered creep on the southern SAF has been reported for nearby moderate to large earthquakes beginning with the 1968 Mw 6.5 Borrego Mountain earthquake (Allen et al, 1972) and for numerous subsequent nearby earthquakes (Williams et al, 1988, Tymofyeyeva et al., 2019, Bilham and Castillo, 2020). Paleoseismic trench investigations indicate a 300-year mean slip rate near Indio of 3.4 ±0.7mm, and 4 ±1 mm near Ferrum (Sieh and Williams, 1990).

Sieh (1986) estimates the most recent major rupture occurred in 1680, whereas Rockwell et al (2018) take into account effects of inundations and conclude that the Coachella Section ruptured in C.E. 1726 ±7 and 1577 ±67 (two sigma). In either case, the mean recurrence time was found to be ~180 years. Almost 300 years has elapsed since the most recent major earthquake, the longest interevent time on record. Geodetic and geologic fault rate estimates are ~ 20 mm/yr near this location, showing close agreement (Tong et al, 2014), implying a potential slip deficit of 6 m since the most recent large event, although Lundgren et al (2009) use GNSS network velocities and ERS interferograms to derive a 17 mm/yr geodetic rate on the southern SAF, which reduces the slip deficit to about 5 m.

Satellite InSAR observations of the southern SAF show evidence of shallow horizontal slip at a non-triggered rate ranging from 2-5 mm/yr. Lindsey et al (2014) show that for 2003-2010 Envisat images the localization of slip varies with the meandering strike of the fault trace, with high localization on transpressive segments and broad (up to 1.5 km wide) shear zones occurring in transtensive segments. Xu et al (2018) examine twenty-five years of ERS, Envisat and Sentinel interferograms and detect rate changes on decadal scales, modulated by large earthquakes. They conclude strong stress changes may cause this variation in shallow creep rates.

Hazard is not limited to the southern SAF, as there is recognized potential for a combined event with the San Bernardino segment and other regional faults. The 2008 hypothetical "Shake Out" scenario earthquake postulated a Mw 7.8 combined rupture from the Salton Sea to Lake Hughes in the San Gabriel Mountains, radiating disastrous levels of seismic energy into the Los Angeles Basin and spawning in rapid succession M7 aftershocks in the Imperial Valley and the Cucamonga Fault bordering the heavily populated San Gabriel Valley (Jones et al, 2008).

This current study focusses on slip triggered by the 2010 El Major Cucapah Mw=7.2 earthquake. It is part of a broader effort to address key questions regarding California seismic hazard, namely: Is the hazard as high as expected from a simple recurrence model? Is the paleoseismic data set representative of Coachella rupture history? What is the significance of creep in assessing rupture potential? How is slip, including aseismic creep, distributed spatially and temporally? What are the implications of slip distribution for inferring the rheology of the shallow crust in the Salton Trough and Coachella Valley? How is slip partitioned between seismic and aseismic processes, and between strands of the San Andreas system? Relevant observation types are increasing rapidly, so this is also an effort to determine the extent to which UAVSAR observations complement paleoseismology, as well as present-day in situ and remote sensing of this critical fault section in a practical way. Airborne radar interferometry provides

broader coverage than field work with far less physical effort, but requires inference of some components of motion due to geometric limitations and sources of interference.

Generalized slip from the 4 April 2010 Mw 7.2 El Mayor Cucapah (EMC) earthquake has been mapped and quantified by Rymer et al, (2010). They hand-measured field-study locations with as much as 18 mm right-lateral slip in the Mecca Hills. They also report for the first time the use of UAVSAR maps of surface fractures in the Yuha Desert near the California-Mexico border, which were used for field identification and quantification of fault offsets. Many of these faults were newly discovered from UAVSAR imagery. Their report states "The approach that proved most rewarding was to use interferograms prepared by NASA's Uninhabited Aerial Vehicle Synthetic Aperture Radar (UAVSAR) to map surface dislocations, then find these sites in the field for visual verification and fault-displacement measurements."

Creep is recorded on the southern San Andreas and Superstition Hills faults during the earthquake and by additional creepmeters installed after the earthquake on some of these newly identified faults (Rymer et al., 2010). Several continuous GNSS stations of the NSF EarthScope Plate Boundary Observatory in the vicinity of the southern SAF record time series breaks at the time of the EMC earthquake, quantifying strain change in the vicinity of surface creep on local faults.

In past work we have reported slip triggered in 2010 on the Imperial, Superstition Hills, and East Elmore Ranch faults, (Donnellan et al, 2014), painstakingly estimated by projected displacements from the UAVSAR interferogram recorded as unwrapped phase. Automatic detection and characterization of surface fracture has been reported (Parker et al, 2018) and estimation of fault slip at depth and fracture zone width is added in Donnellan et al (2018) to track continuing slip on the Yuha fault and the Ocotillo extension of the Elsinore fault over a seven-year period using many interferograms.

Table 1 lists the UAVSAR products highlighted in this work. Line 08517 overlaps some of line 26516 and also shows evidence of intermittent slip seen from the conjugate direction (looking north), not presented here. Line 26518, parallel to 26516 and adjacent to the north, does not show evidence of EMC coseismic slip on the SAF.

Table 1. UAVSAR data products, dates.

UAVSAR product name	Visit1	Visit2	PixelToRadarBearing
SanAnd_26516_09015-010_10028-007_0354d_s01_L090HH_01	24Apr2009	13Apr2010	355
SanAnd_26514_09015-001_10028-005_0354d_s01_L090HH	24Apr2009	13Apr2010	355

In following sections, we summarize interferometry records of slip triggered by the El Major Cucapah earthquake. We infer this slip to have been induced by shaking accompanying the passage of surface waves from the earthquake. We then present mapped slip on the southern SAF as observed by UAVSAR repeat-pass unwrapped interferograms, including a detailed comparison of the automated characterization of subsurface slip and fault-zone width with many displacement profiles taken across the SAF in the Mecca Hills. Triggered slip is detected and estimated from a second UAVSAR interferogram, covering the receding shore of the northern Salton Sea.

Creepmeter and GNSS measurements

The surface ruptures of the EMC earthquake are shown on Figure 1, together with the trace of the southern SAF and the Imperial Fault. The figure also shows the location of creepmeters (Bilham and Castillo, 2020), GNSS permanent stations, and the Table 1 UAVSAR data images spanning the date of the earthquake.

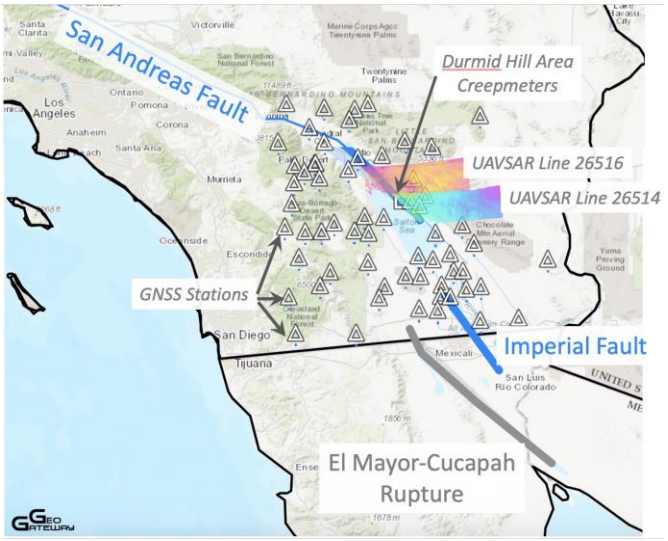

Figure 1. Southern SAF, Imperial Fault (blue), and EMC rupture (gray). Durmid Hill area creepmeters (locations in Figure 6), arrowed. GNSS stations=triangles.

Creepmeter time series near the time of EMC and GNSS 3-d deformation between 24April2009 and 13April2010 (the dates of UAVSAR observations) are shown in Figure 2. GNSS displacements for the time period between the radar visit dates are displayed in Figure 2(b&c) using the GeoGateway GNSS tool (Heflin et al, 2020). The horizontal GNSS vectors indicate a pattern of coseismic dextral strain across the Coachella Section of the SAF, and also a pattern of relative vertical motion across the Coachella Valley, downward on the west side, and a strong pattern of coseismic uplift in the entire Salton Trough, particularly at the south end.

GNSS relative motion between the sites P491 and P607 for significant time spans are listed in Table 2. These two sites (Coachella Valley and NE of Mecca Hills), span the area of interest. While both stations move about 14.5 mm to the south within a day of the earthquake, what matters for coseismic strain in the SAF vicinity is the relative motion, and this is insignificant (1.1±1.2 mm). Table 2 shows this relative motion of the two sites spanning the radar visits (Figure 2b) is dominated by the tectonic velocity. The displacement arrows in the northern part of the figure similarly reflect 354 days of tectonic motion, while the displacements in the southern part are dominated by coseismic motion.

Seismicity in the radar visit time span has been investigated with the GeoGateway Seismicity Tool (Donnellan et al, 2021), which uses the USGS catalog service at https://earthquake.usgs.gov/earthquakes/map/. There are no catalog earthquakes >Mw 2.5 within 10 km of the SAF within the area covered by radar lines 26516 and 26514.

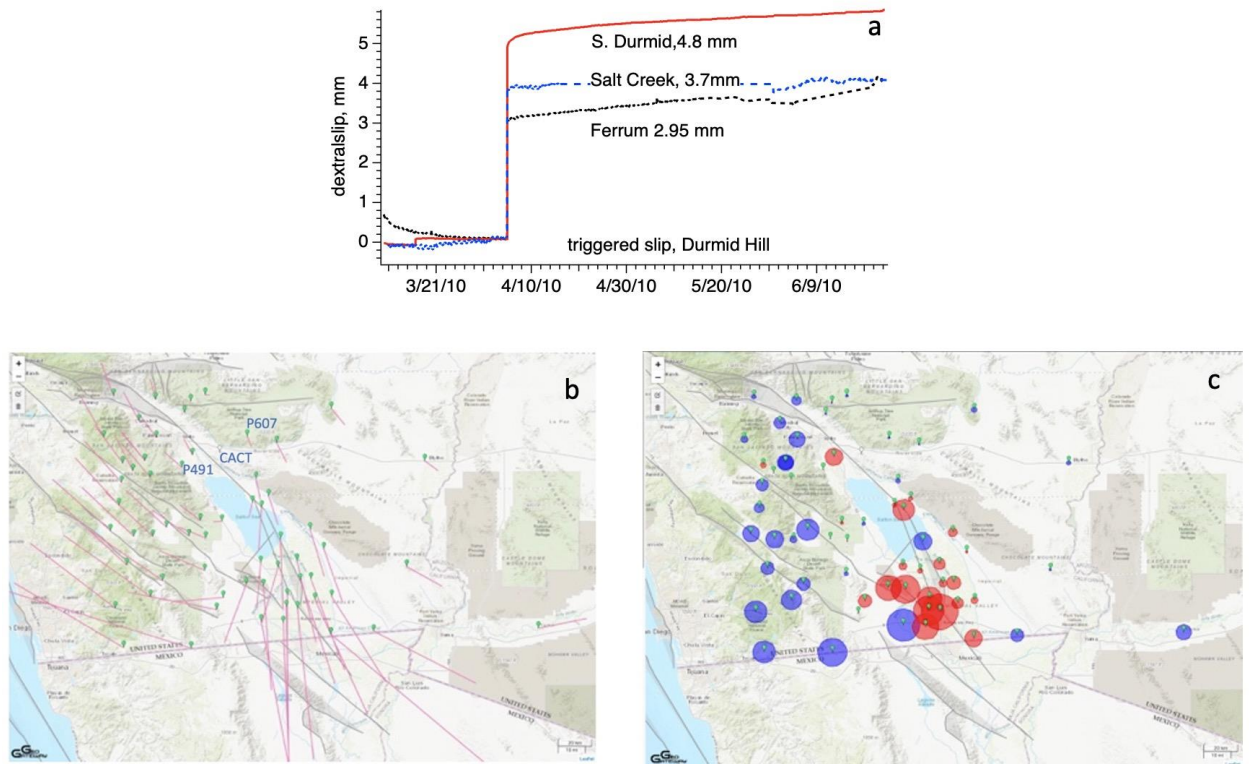

Figure 2. Creepmeter and GNSS products. (a) Creepmeters recorded extension (at 30° obliquity to the fault) ~3-5 mm between contiguous 5-minute samples at three locations on Durmid Hill. Minor additional slip (<0.2 mm) occurred in the following few weeks. (b & c): GNSS station displacements corresponding to dates of UAVSAR visits 2009Apr24, 2010Apr13 bracketing the EMC earthquake with fixed station CACT, east of the Coachella Valley. (b) Horizontal component indicates dextral shear imposed on southernmost SAF. P491 and P607 record 14 mm dextral shear. (c) vertical displacement. Red signifies upward motion, blue downward; largest red circle indicates 15 mm upward. Region to west of Coachella Valley is displaced downward ~10 mm, region to east shows little motion, while Salton Trough is displaced upward, particularly south of the Salton Sea (~15 mm).

Table 2. Relative motion between GNSS stations P471, P607, with formal errors.

Station	*Timespan*	*DeltaE(mm)*	*DeltaN(mm)*	*Amplitude(mm)*	*Comment*
P491	Coseismic: 04Apr2010	-0.04±0.8	-14.5±1.0	15	Estimated break
P607	Coseismic: 04Apr2010	1.1±0.8	-14.6±0.9	15	Estimated Break
P607 – P491	Coseismic: 06Apr2010-02Apr2010	1.1±1.2	-0.0 ± 1.4	1.1	From model fit to time series
P607 – P491	RadarVisits: 24Apr2009-13Apr2010	8.7 ±0.4	-10.7±0.5	13.8	Using 10-day mean positions (Figure 2)
P607 – P491	Velocity > 15 years	8.5±0.2	-11.0±0.2	13.9	Annualized over station lifetime, excluding breaks

2. Surface fracture characterization by image analysis

UAVSAR unwrapped repeat-pass interferograms (RPI) indicate the radar line-of-sight component of relative displacements across the image. Each sample corresponds to a 6 m pixel footprint at mid-latitudes. Consecutive images on a repeating linear flight path reveal changes to the landscape between the dates of the radar flights. For the formation of interferometric fringes, the first flight path must be repeated by succeeding flights to within a distance of 5 m (Hensley et al, 2009). This is made possible by a custom autopilot system guided by GPS real time positioning on-board the aircraft (Hensley et al 2008). This NASA UAVSAR system has unique capabilities compared to satellite InSAR systems: flight lines may be arbitrarily configured to provide near-optimal measurements of crustal processes, including earthquakes and triggered slip associated with active surface tectonics. Ionospheric interference is avoided by flying at stratospheric altitudes, a comparatively low vantage point that allows high resolution imagery. Noise in the UAVSAR system is chiefly from unmodeled atmospheric refraction and residual errors in flight path positioning. These effects are characterized by > km-scale variations in recorded phase, and so are largely canceled in the estimation of shear near a fault.

In past work we have developed image analysis using the Canny computer vision method (Canny, 1986) for edge detection to determine candidate pixels for characterizing surface fractures. We employ the *Python OpenCV* module for this. Initial development and results characterizing triggered fault slip are described in Parker et al. (2018). That work documents automatic estimates of slip induced by the El Major earthquake on minor faults in the Yuha Desert of California, detection of postseismic slip on the Yuha fault and detection of a previously unknown transition fault connecting the Laguna Salada fault with the Elsinore fault. It also reports on the initial detection of coseismic slip on the southern SAF (in line 26514) and estimates coseismic and triggered slip in the 2014 M6.0 South Napa earthquake. A refinement of the method and its application to the estimation of seven years of afterslip on the Yuha Fault and the Laguna Salada-Elsinore transition fault are reported in Donnellan et al. (2018).

The current method explores analysis of UAVSAR RPI phase-displacement images in five stages, listed in Table 3. Key stages are illustrated in Figure 3. These stages are uniformly applied in this work with parameters shown in Table 4.

Analysis in this section reports the radar view of slip, s_R: the radar is sensitive to the component of displacement aligned with the line of sight from the ground patch to the aircraft. Because the aircraft views the ground from a known elevation angle e and azimuth, and the azimuth is misaligned with the fault strike by Δa, a hypothetical purely dextral slip s_D will be viewed as $s_R = s_D \cos(e)\cos(\Delta a)$. In Figures 3-7 the plotted slip is s_R, while inferred dextral slip s_D is reserved for the Discussion and Figure 8.

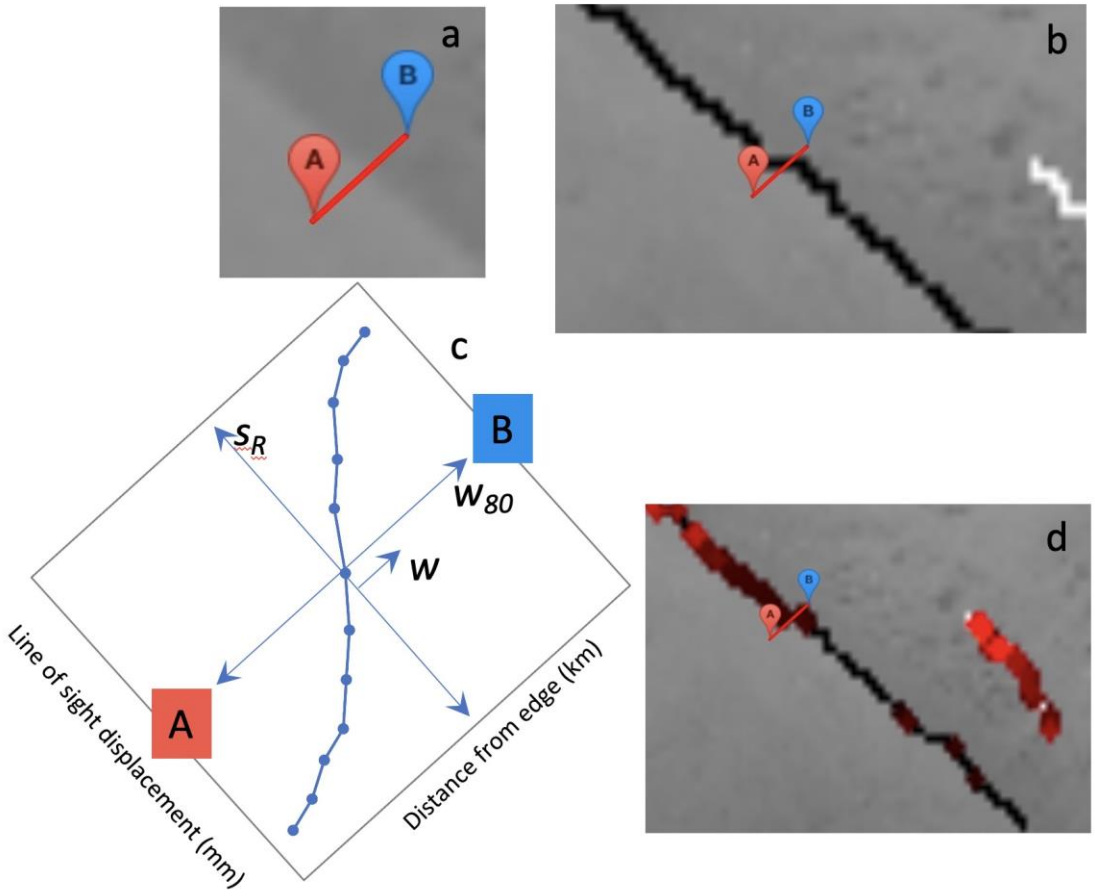

Figure 3. Illustration of edge-detection process and the subsequent derivation of slip and width. (a): image preparation produces high-contrast grayscale image. Line AB is projected across each detected edge. (b)- Slip polarity: Canny-determined edge is colored black corresponding to dextral slip and white for sinistral slip. (c): definition of radar-viewed slip and width quantified for each detected local shear feature. (d): Radar-viewed slip amplitude: Localized slip is color-coded according to slip amplitude (scale indicated in Figure 4)

Table 3. Image processing stages generating edge detection/surface fracture maps and tables

Stage 1	Read line-of-sight radar displacements from unwrapped ground-range UAVSAR file.
Stage 2	Prepare image: determine missing or rejected pixels, fill with smooth values.
Stage 3	Use global *Canny* algorithm to find list of edge-bearing cells, candidates for surface slip.
Stage 4	Examine environment of each edge cell: evaluate along-gradient samples, and generate KMZ map of sense of slip.
Stage 5	Iteratively find width and amplitude: create table, KMZ partially transparent image.

Table 4. Image processing parameters.

Rejection threshold, mean coherence *(Stage 2)*	< 0.3 over 18x18 cells
Rejection threshold, displacement standard deviation *(Stage 2)*	< 7 mm over 18x18 cells
Pre-canny smoothing kernel *(Stage 2)*	18 cells
Coherent down sampling *(Stage 2)*	5x5 cells
Canny aperture size *(Stage 3)*	5 down sampled cells
Canny threshold *(Stage 3)*	5 mm
Canny hysteresis ratio *(Stage 3)*	0.75
Along-strike averaging *(Stage 5)*	None
Local inflection slope ratio threshold *(Stage 5)*	0.2
Slip KMZ image color lower saturation point *(Stage 5)*	5 mm
Slip KMZ image color upper saturation point *(Stage 5)*	20 mm

2a. Slip on UAVSAR line 26516 near Mecca, California

Figure 4 shows the sense of slip with the area of consideration for line 26516, and the final slip amplitude map. The sense of slip is analogous to the classic test of strike-slip fault motion, adapted for the radar viewpoint. The radar views the surface at an oblique angle, looking left referenced to its flight path. Flight line geometry and the sign of the phase gradient at detected edges are used to determine the sense of slip. As the radar views the environment of a detected edge, there must be relative displacement between the two sides adjacent to the edge. If the right side in the radar view is moving toward the radar, the edge is colored black, consistent with right lateral motion across a surface fracture. If the left side is moving relatively toward the radar, the edge is colored white, consistent with left-lateral motion. For the single-view images shown here, the radar cannot distinguish strike-slip from dip-slip motion. For edges corresponding to pure strike-slip motion, the black-white coloration of edges is a reliable indicator of the sense of that strike-slip motion, right or left lateral. Note in Figure 4a that nearly all detections on the SAF are colored black, indicating the triggered slip (when purely strike slip) is consistent with dextral motion.

A significant fault left stepover occurs at the mouth of Painted Canyon: SE of a gap at Painted Canyon dextral slip continues on a fault strand displaced 200 m NE. An oblique white crossing edge appears to mark the edge of the Painted Canyon alluvial fan. Also note near North Shore, at the south-east end of this SAF portion there is indication of multistranded triggered

slip. Detected edges to the southwest of the SAF are chiefly associated with man-made structures and agricultural field edges, while detected edges to the northeast occur in extremely rugged terrain, and may correspond to few-cm landslides, ridge spreading, bedding-plane slip or differential settling. Contorted and folded beds on Durmid Hill showing evidence of recent surface disturbance are mapped by Jänecke et al, (2018). Similarly, disturbed bedding planes are probably observed by UAVSAR in a subsidiary damage zone from the M5.2 La Habra earthquake (Donnellan et al, 2015). In the following we ignore features more than 500m from the SAF, to focus on triggered slip and associated off-fault deformation.

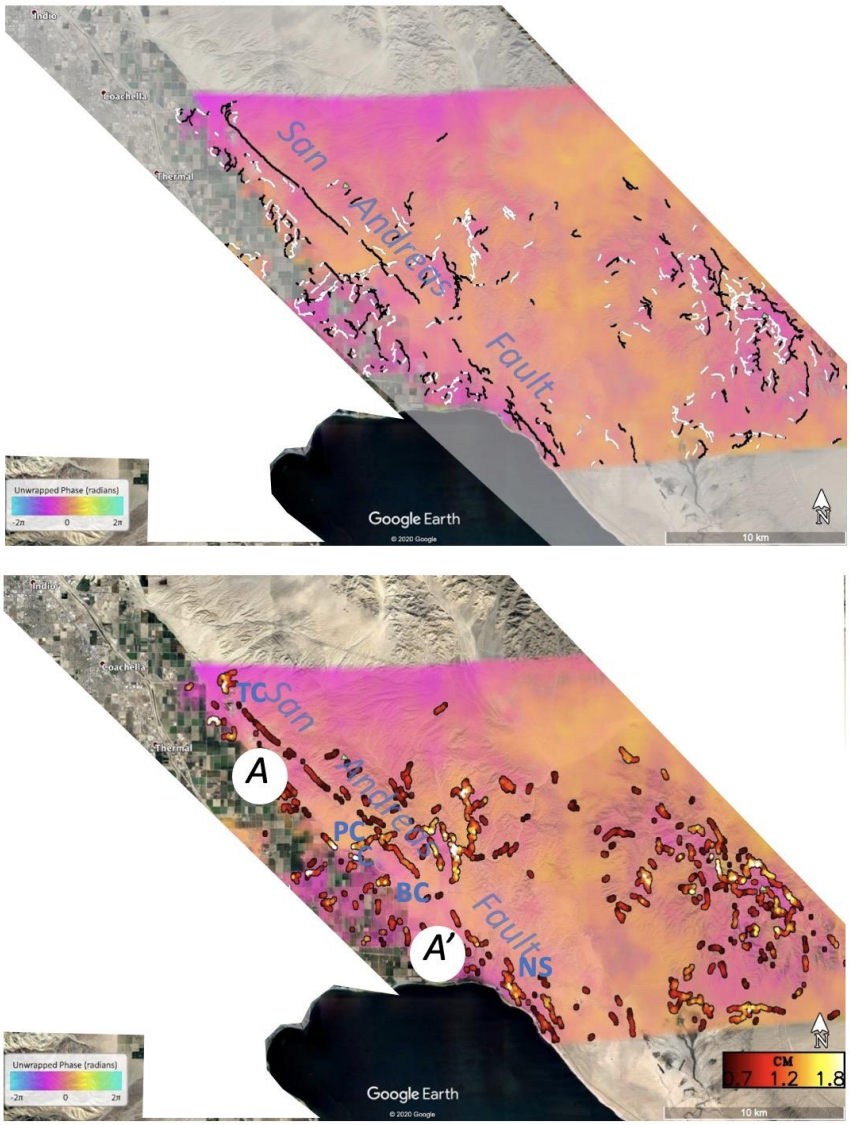

Figure 4. Portion of line 26516 coseismic interferogram in the vicinity of the SAF. (a): Polarity of slip, black dextral, white sinistral. Data are quantified within 20-km-wide swath of light shading parallel to SAF. (b): Radar-observed amplitude of slip on localized shear zones coded according to 5-20 mm scale at lower right. Mapped fault shows as discontinuous throughgoing line between TC (Thermal Canyon) and NS (North Shore). PC: Painted Canyon, BC: Box Canyon. Portion from *A* to *A'* is detailed in Figure 5.

Figure 5 shows a 14-km selected segment of the SAF through the Mecca Hills, part of UAVSAR line 26516. The selection focuses on an area of intermittent slip, illustrating off-fault displacement for surface breaks, gaps, and shear zones. The panels represent the resolved components of width and slip for features identified in Figure 4b within about 500 m of the mapped fault trace (a limit chosen to minimize interference from man-made disturbances such as agricultural development). Continuous series are plotted at 500-m intervals orthogonal to the fault generated from the line 26516 inteferogram data using the UAVSAR line-of-sight profile tool of the GeoGateway application (geo-gateway.org). The width is parameterized as though the sigmoid were proportional to arctan(x/w) where x is the fault transverse distance. Note that estimated slip is the relative projected displacement across the entire detected shearing zone (Figure 3c), whether that resembles a step function or a sigmoidal curve. The arctan function (characteristic of buried elastic faulted slip) has a rather slow asymptotic approach to the region of full slip, so this reported width will typically be smaller than a visual estimate of the shear zone width. Evaluation of the arctangent function shows that 80% of the total shear displacement is contained within a band of width $w_{80} = 6w$, where w can be shown to represent the approximate depth to the top of subsurface dislocation in an elastic half-space (Savage and Prescott, 1978).

The information explicit in aligned panels of Figure 5 facilitate a partial validation of our automated estimates of slip and width. In the third panel the two left-hand profiles appear noisy, and correspond to spatially interrupted detection of the slip depicted in Figure 4. The next four profiles (when due allowance is made for the spatial smoothing involved in forming the profile) show discrete localized offsets, indicating slip indistinguishable from rupture of a surface fault. The next three profiles show smaller jumps, close to the threshold of the image analysis and corresponding to intermittent slip markers on Figure 4. Profiles near the middle clearly indicate a broader shear zone, consistent with the larger width estimate cluster and also the larger slip values: the slip estimate embraces the total amplitude of the sigmoid characterizing the shear zone. A few points show detected slip from about 10-12.5 km from the start (the northwest most considered profile), corresponding to the noisy profiles that show no obvious trend. The last two profiles show a restoration of a broad trend, corresponding to the final cluster of ~10 cm slip across a ~50m width. These broader zones of deformation found at the end of the segment correspond to the distributed shear described between transpressional segments described by Lindsey et al., 2014).

2b. Slip on UAVSAR line 26514, northeast flank of Salton Sea

Figure 6 shows the sense of slip, area of consideration, and slip magnitude estimates for line 26514, similar to Figure 4. This map is more complex, as we find in addition to SAF slip several other features highlighted by edge detection. The first right-lateral lineation NE of the SAF marks the Hidden Spring fault. Mixed-sense parallel lineations just east of the SAF farther south correspond to edges of a dry wash, that may have experienced coseismic settling. Other connected strands are associated with sloping sides of irrigation canals and hydrologic structures associated with this network of canals.

Figure 7 shows the width parameter w and radar-view slip s_R for points in Figure 6c selected to lie within about 500 m of the SAF trace. Note there are several consistently slipping sections, interrupted by gaps at reference point distances 2-3, 6-7, and smaller gaps at 11 km and 14 km.

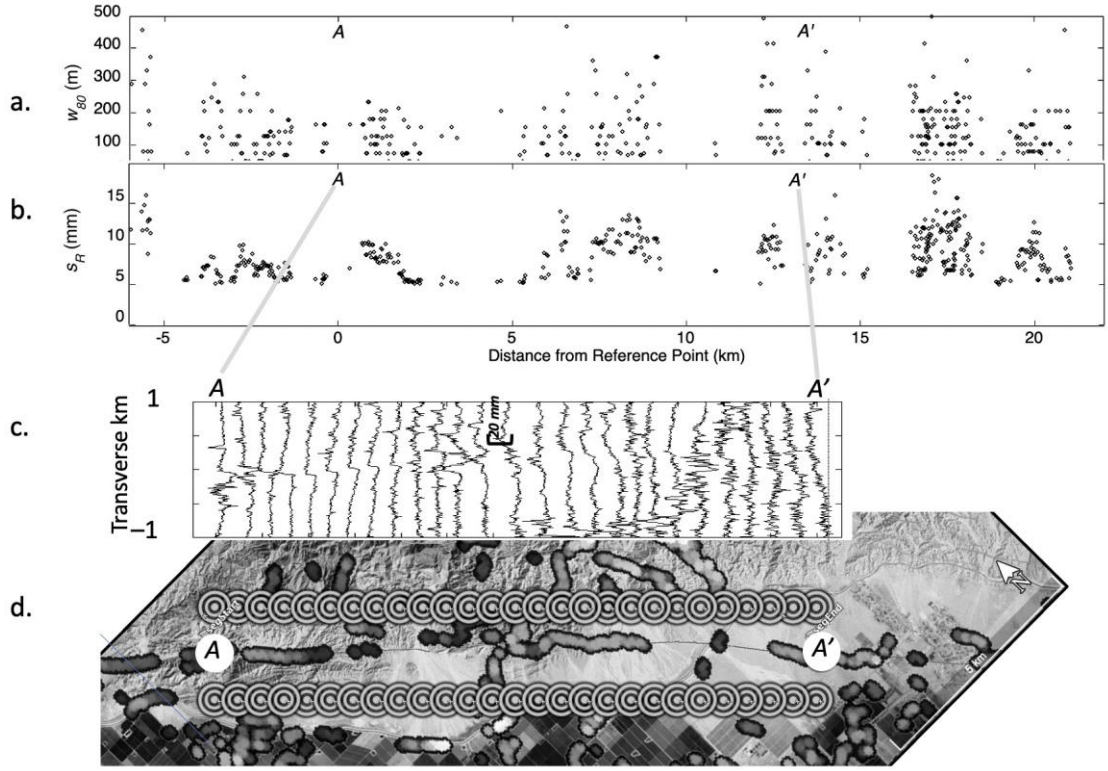

Figure 5 Mecca Hills segment of SAF. (a) Width parameter w and (b) radar view slip s_R for edges detected within 1 km of mapped fault. (c) 2-km-long line-of-sight displacement profiles normal to fault extracted using GeoGateway UAVSAR line of sight tool. Positive displacements imply ground position change toward the aircraft. Each 500 m spaced profile is the average of three contiguous profiles spaced at 50 m intervals. (d) Google Earth map view indicating start and end points of profiles in (c). Reference point is the on-fault target at 116.057539°W, 33.633535°N

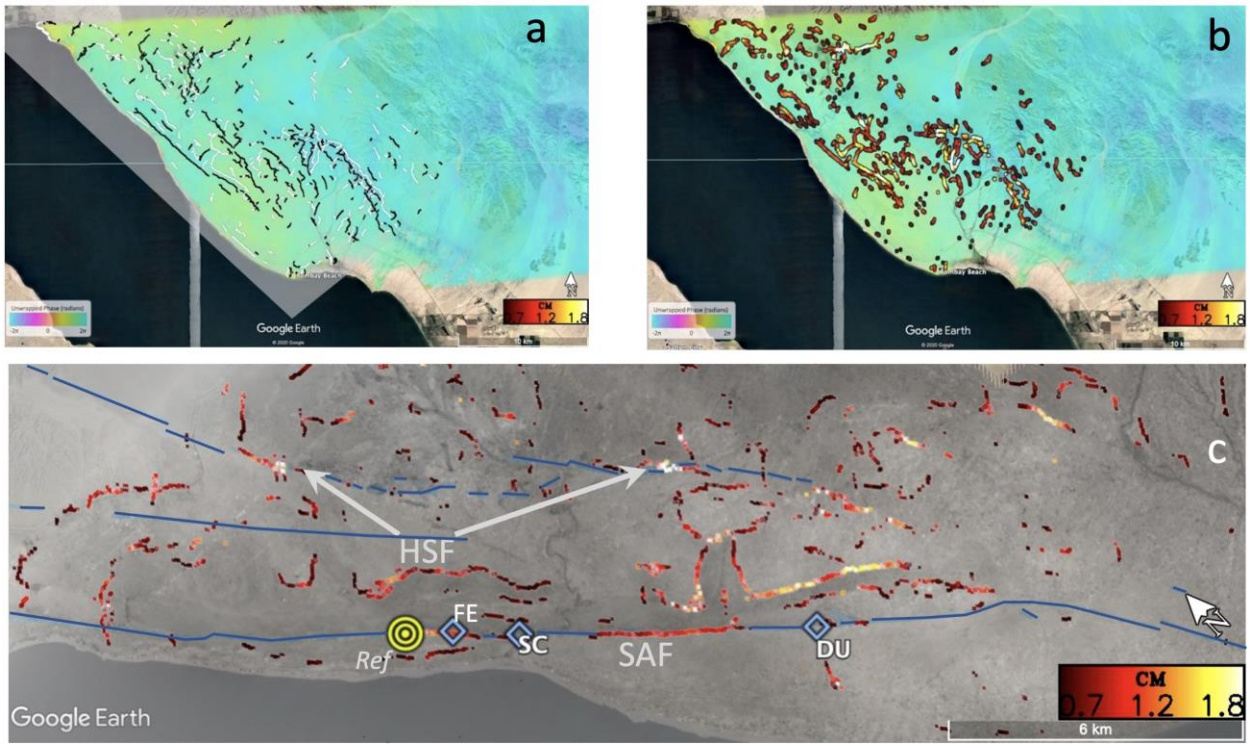

Figure 6. Durmid Hill segment of southern SAF (26516 coseismic interferogram). (a): polarity and location of detected edges, black dextral, white sinistral. (b): slip amplitude relative to radar line of sight. (c): Fault parallel view, of grayscale interferogram and heat-colored slip amplitudes (scale lower right), with fault traces from Quaternary Fault and Fold Database of the United States, blue. (earthquake.usgs.gov/static/lfs/nshm/qfaults/qfaults.kmz). Creepmetes FE: Ferrum, SC: Salt Creek, DU: Durmid Hill. HSF: Hidden Spring Fault, SAF: San Andreas Fault.

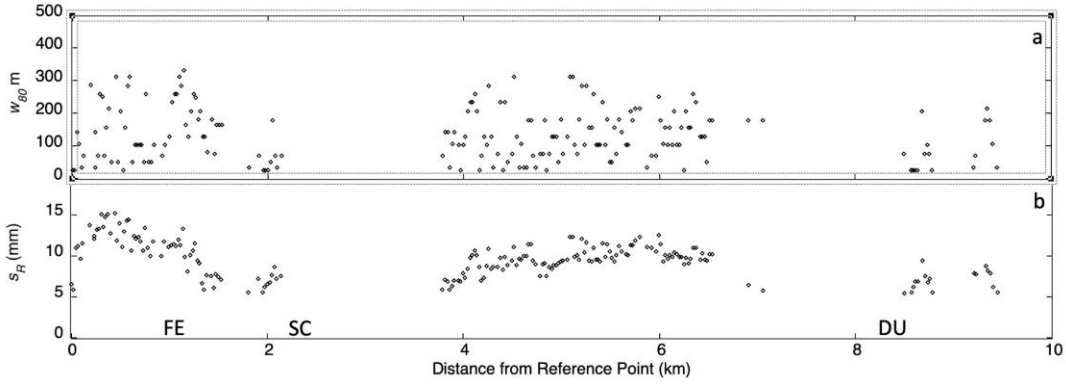

Figure 7. Line 26514 sigmoid parameter fault motion estimates along the Durmid Hill segment, southern SAF, vs. km (SE) from reference point at 115.86194°W, 33.462845°N (yellow target icon in Figure 6c).Fault parameters as determined according to Figure 3, and same as Figure 5(a&b) (a) Shear zone width parameter w_{80}. (b) Radar view of shear (slip) s_R on SAF. Radar view slip below 5 mm is not quantified. Creepmeters indicated FE, SC and DU

3. Discussion

Our numerical estimates for localized off-fault slip and width indicate significant variation. Even on well-known faults, slip is discontinuous and separated by km-scale gaps. The scatter is partly inevitable as we are working close to the noise-level of our observing method. We do not quantify radar-view slip less than 5 mm. Comparisons with field measurements of triggered surface elsewhere (Parker et al, 2018) suggest that estimation error for radar-view slip s_R in moderate terrain with little vegetation is of the order of 8 mm, while in some heavily vegetated settings such as the Napa Valley, the bias plus random error is closer to 40 mm. The updated method used here appears to have random error ~0.3 mm based on sample variance for a 1 km subsegment (1.2-2.2 km from reference point) in segment 1 in Figure 5.

The shear displacements s_R in Figures 5b and 7b integrate shear to a distance of at least w_{80}, exploring a fault-centered band until sufficient samples are included to estimate arctangent profile, parameterized as slip and width. Hence over 80 % of the estimated slip is directly measured in terms of radar line of sight displacement, and the remainder is supplied by evaluating the asymptotes of the arctan function that fits the data. Considering the SAF in interferogram 26514, we base our estimates on samples within 60 m or more of the fault for narrowest width transition zones, and within 300 m for the widest that are encountered. For the mean width transition where w = 22 m, elastic dislocation theory would imply the approach of subsurface slip on a discrete dislocation to within 3-5 m of the surface of a half space. We discuss the consequences of this subsurface slip in a following section. Although our width estimates are spatially smoothed by our averaging algorithms, and therefore may represent much narrower zones, some ≈3-km-long segments of the fault clearly show >100-m-wide (w_{80}) shear zones. In these broader locations multiple surface fractures are evident, some at oblique angles to the strike of the main fault. The kinematic behavior of these short segments is probably controlled by local structures, minor transpressive or transtensive features along-strike, or variations in fault rheology in the uppermost several hundred meters of the fault.

From the radar view of slip in Figures 5b & 7b we interpret the UAVSAR data as dextral slip s_D and compare it to triggered slip mapped during post seismic fieldwork reported by Rymer et al., (2010) in Figure 8. Since the radar views the scene from above, actual dextral slip may be larger or smaller if dip slip is present, although none was reported at sites mapped by Rymer et al., (2010) and we neglect that possibility here. In Figure 8a we project the UAVSAR data as dextral slip together with triggered dextral slip mapped during post-seismic fieldwork following EMC (Rymer et al., 2010).

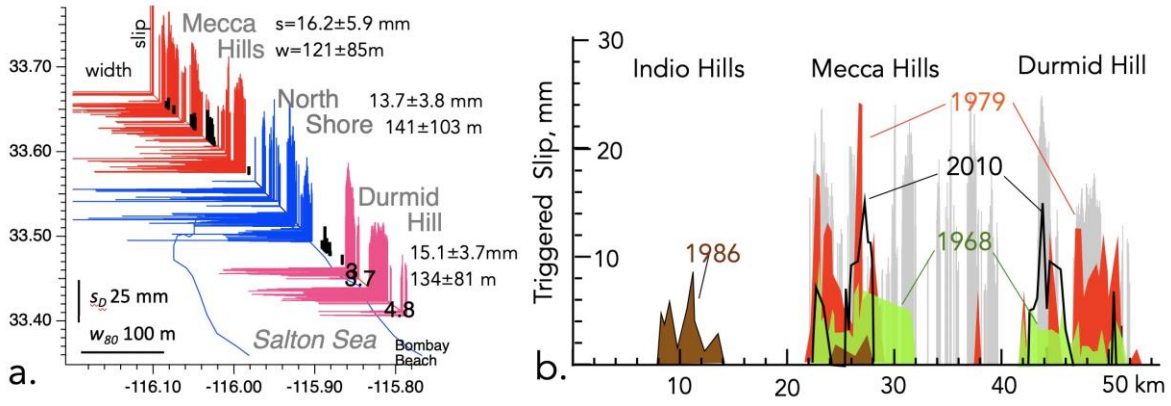

Figure 8. Radar observations compared with field measurements. (a) Radar observations of dextral slip and surface shear zone width compared with field measurements of 2010 triggered slip (black bars). Numerical averages for three identified segments of the fault are listed in the figure. Black numbers indicate slip (in mm) recorded by creepmeters. (b) Mapped triggered slip in the 2010 earthquake (black line) is less extensive and numerically averages half that calculated from UAVSAR imagery (grey), and suggests that previous triggered slip (Williams et al., 1988) associated with earthquakes in 1968, 1979, 1986 has been underestimated.

Several studies indicate that triggered slip on the southern SAF is confined to transpressional segments of the fault, each approximately 12.5 km long and separated by intervening right-stepping segments with strike closer to the plate boundary slip vector (Bilham and Williams,1968; Williams et al., 1988; Lindsey et al., 2014). The UAVSAR data indicate that triggered slip in 2010 occurred on these transpressional segments but also within the intervening North Shore segment (Figure 8b). Lindsey et al., (2014) report a broad >200-m-wide shear zone in this segment. Our data show also that in addition to fault slip, off-fault deformation occurred over a wide region throughout the Mecca Hills and Durmid Hill, and that minor slip occurred also on the Hidden Springs fault to the north of the SAF.

Triggered slip accompanies the passage of surface waves from distant earthquakes (Bilham and Castillo, 2020), and releases strain stored near the shallow fault imposed by plate boundary shear stresses. The incremental static strain from EMC at Durmid Hill is insignificant compared to fault zone shear strain responsible for creep rates in the valley (Table 2), although Xu et al. (2018) reveal that it may influence subsequent slip rates on the fault. The rate of surface creep is governed by the ratio of the depth of surface slip to the depth of base of the seismogenic zone and the applied regional shear strain rate. Sieh and Williams (1990) inferred a depth for creep of 1.6±0.6 km. Our finding that off-fault dextral triggered shear may equal that recorded as slip on the fault, would need this slip depth to be doubled, however, it is possible that non-triggered creep may be restricted to shallower depths.

3a. Durmid and Mecca Hills mapped surface slip compared with UAVSAR slip.

Where surface mapping and UAVSAR data overlap, triggered dextral shear is underestimated by surface observations. In the Mecca Hills the mean UAVSAR-derived triggered slip in 2010 was 16.2±5.9 mm and on Durmid Hill it amounted to 15.1±3.7 mm . These are consistent with the maximum mapped slips of 18 mm and 15 mm respectively, but are

73% and 47% larger than the average observed surface offsets of 9.5±4.6 mm and 7.1±3.7 mm respectively. Since mapped slip reported in 2010 was similar in amplitude and spatial distribution to mapped slip triggered by previous nearby earthquakes, it follows that previous estimates of triggered slip were also underestimated.

A possible systematic bias for underestimating fault slip in field mapping follows from a unique observation in the 2004 Parkfield earthquake. Surface afterslip was undetectable at Work Ranch on the southern segment of the surface rupture until strain in the soils overlying the surface fault exceeded approximately 400 μstrain (Bilham, 2005). This was recorded by a creepmeter as subsurface extension gradually increasing over 3 days to 5 mm. It is thus probable that fault slip below 5 mm in the fault zone during triggered slip in 2010 left no visible evidence for surface offsets. Where they were visible, the 2010 offsets consisted of discontinuous en-echelon cracks following the fault zone, often curved and rarely parallel to the strike of the fault (Rymer et al., 2010). These are suggestive of shear strain rather than localized surface rupture.

Consistent with this inference is the observation that no surface offsets occurred on the surface fault above any of the creepmeters (Rymer et al., 2010) despite quantitative records for the timing of 3-4.8 mm subsurface extension across the fault zone at just 0.5 m depth (Figure 2a). In 2017 near creepmeter SC during a succeeding triggered slip episode, a distinct line of slip was observed at depth in a 3-m-deep gully that could not be followed to the surface (T. Rockwell, personal communication, 2021). The simplest interpretation of the absence of mappable surface slip is that surface strains were insufficient to crack surface soils, and that the signal measured by the creepmeters was not fault slip but fault zone shear strain. The maximum strain recorded by the southernmost creepmeter in 2010 was 343 μstrain (4.8 mm in 14 m).

3b. Near-surface fault rheology and changes in surface locking depth 2004-2020

Hitherto creep in the Coachella valley has been assumed to extend from the surface to depths of the order of 1.6 km based on long term creep rates (Sieh and Williams, 1988), or ≈2.5 km from detailed studies of triggered slip (Timovyeyeva., et al., 2018). These studies characterize the depth of the transition from the locked seismogenic fault to the base of the creeping zone as the upper locking depth. We now introduce the notion of a *surface locking depth*, a depth below the surface above which the shallow fault is locked. The existence of a surface locking depth for creep on segments of Durmid Hill is implied by the absence of surface slip, and the consequences of reconciling the numerical observations of antisymmetric shear strain (width and slip from UAVSAR), and observed strain (inferred from embedded creepmeters). If we consider the fault embedded in elastic half space underlain by a planar dislocation we can solve for this locking depth.

The concept of a locked surface fault is an apparent contradiction. Clearly the surface fault does indeed slip during earthquakes. However, during the interseismic period, creep and triggered slip, which behaves at depth as planar slip on a distinct fault surface penetrates through this surface layer as a distributed shear zone meters to tens of meters wide. The assumption of planar slip at shallow depth provides a starting point for interpreting the observed fault slip behavior 2004-2020.

445 **Table 5**. First row indicates mean UAVSAR observed width and dextral-shear for the Durmid
446 segment of the SAF. The remaining three rows apply to creepmeter locations, and calculated
447 surface locking depth and width for subsurface creep.

location	s_D (mm)	$creep_{obs}$(mm)	$depth_{calc}$(m)	$width_{calc}$ (m)	w_{80} (m)
$DURMID_{AVE}$	15.1	4.8	13.4	80	134±81
DU	8.0	4.8	6.3	38	51±26
SC	12.9	3.7	15.0	90	52±51
FE	18.7	3	27.4	164	165±35

448

449 To calculate local locking depths, we use UAVSAR observations of triggered shear width
450 and dextral shear amplitude closest to each of the creepmeters (Table 3). For applied dextral
451 shear of 8 mm and deformation width of 51±26 m (the two closest UAVSAR observations) we
452 determined analytically a surface locking depth of 6.3 m and shear zone width of 25 m (Figure
453 9a). For a different time span Lindsey et al.,(2014, Figure 5a) calculate a fault zone shear width
454 for this location of 110±50 m implying an ≈18 m deep surface locking depth. Calculations at the
455 other two creepmeter locations using local UAVSAR estimates for applied triggered shear and
456 width yielded dislocation depths of 15 m at Salt Creek (SC) and 27 m at Ferrum (FE).

457 The result implies that the surface fault includes a tough carapace whose rheology can
458 sustain shear strain but is resistant to throughgoing slip. This unexpected result resembles the
459 behavior of shallow coseismic slip and afterslip on the West Napa fault described by Brooks et
460 al, (2017). Brooks et al (2017) found that >1 m of coseismic slip failed to rupture the surface but
461 terminated at 3-25 m depth subjecting surface materials to distributed shear. Our inferred
462 subsurface slip is two orders of magnitude less than theirs but the geometry appears to be similar.

463

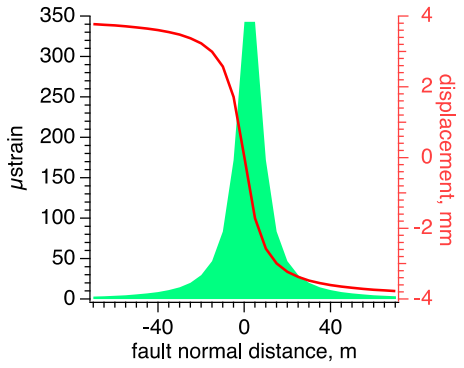

464

465 **Figure 9.** Antisymmetric fault zone displacements and creepmeter-measured strain as a function
466 of distance from a creeping fault locked below 6.3 m depth subjected to 8 mm of applied shear
467 (Table 1). 80% of the shear occurs within a 38 m wide zone (≈6 times the locking depth).

468 The surface fault that we encountered while installing the creepmeters consists of a 3-5 m wide
469 foliated gouge zone consisting of interleaved phacoidal clasts (Vanucchi, 2019) with dimensions

of 2-20 cm. We propose that the ensemble response of these clasts is to act as a buffer to inhibit planar subsurface slip from surface expression as a linear break. We envisage that the surface fault severs a path through these clasts only in major earthquakes or in occasional creep-events. Thus, what has hitherto been interpreted as interseismic creep on the surface above the fault is distributed strain caused by rearrangement and rotation of the clasts in the fault zone. In this scenario the creep-meters record strain, not fault offset.

A shallow slip-resistant layer accounts for the surface expression of creep on Durmid Hill during previous triggered episodes as discontinuous en-echelon cracks. A similar surface layer was reported by Scott et al., (2020) at Dry Creek. Rarely, slip is manifest on the southernmost SAF as an almost continuous line of surface cracking, as was triggered by the 2017 Chiapas earthquake (Tymofyeyeva et al., 2019, supplement S9). Occasional surface failure of the surface-resistant layer evidently occurs if we are to explain the apparently discrete offset of berms, channels, shorelines, concrete structures and rail lines (Sieh and Williams, 1990; Blanton et al., 2020). The fault-normal width of these long-term offsets varies from 8 cm to 2 m. In the case of the S. Napa fault subsurface coseismic slip penetrated through to the surface as afterslip, annulling most of the observed slip deficit. On Durmid Hill no afterslip occurred.

Our measurements address the important question of how effectively long-term dextral surface creep of the fault is characterized by measurements of discrete offsets of the surface fault and creep measurements, and whether these numerous fault observations can be corrected empirically to more accurately evaluate subsurface slip. One potential difficulty in addressing this issue is whether the broader deformation we observe during triggered slip is representative of deformation during slow aseismic slip between triggered events. Our proposed model is testable in that the width of the surface deformation zone provides a measure of the variable thickness of the rheological carapace that inhibits discrete surface slip. The width of the zone is approximately 6 times the thickness of this layer. However, given a creep rate of 2 mm/yr an empirical correction will only be quantifiable with UAVSAR measurements only after several years of measurement.

A larger earthquake hazard assessment issue arises if off-fault deformation is substantial during major earthquakes on the southern SAF. Studies of deformed and deflected drainages through the Mecca Hills reveal that long-term deformation is accommodated by non-recoverable plastic shear absorbed to distances of several km from the surface fault (Gray et al., 2018). If this prevails it would render paleoseismic estimates of slip (derived from ≈10-m-wide trenches across the fault) lower than slip at depth, as proposed by Grant and Donnellan (1994) from measurements of the SAF in the Carrizo Plain. Our current UAVSAR data provide a spatial foundation from which these effects may be quantified in a future earthquake.

4. Conclusions

We investigate the utility of UAVSAR remotely-sensed repeat pass interferometry line of sight displacement maps for identifying and characterizing triggered fault slip on the southernmost San Andreas Fault, in the context of geological mapping, creepmeter data and GNSS records.

All pixels on recognized SAF traces detected by auto-edge detection methods are consistent with dextral shear. Slip is spatially discontinuous and has variable amplitude along strike. The width of triggered shear in some places is indistinguishable from discrete fault slip,

but in many places, it exceeds 125 m and, in some patches, approaches 250 m. Regardless of shear-zone width, projected slip estimates are in the range 5-18 mm, with the caveat that values of slip s_R less than 5 mm are ignored since they are close to the noise level in the measurements. Corresponding inferred dextral slip average ≈15 mm with a high of 16.6±6 mm in the Mecca Hills and a low of 13.7±4 mm in a segment near North Shore where triggered slip has hitherto not been detected. Compared to geological mapping shortly after the 4/4/2010 EMC earthquake, the UAVSAR measurements indicate both more widespread along-strike slip, and a broader zone of deformation, including slip on numerous subsidiary features near the fault. We conclude that distributed shear may have been associated with previous episodes of triggered slip and not been recognized in these regions.

A surprising finding deduced from the combination of radar and creepmeter measurements on Durmid Hill is that creep and triggered slip are a surface expression of planar slip in the shallow subsurface. We introduce the concept of a surface locking depth, above which the surface is locked during creep or triggered slip, to distinguish it from the base of the creeping fault which defines the top of the seismogenic zone. Triggered aseismic slip extends from the upper locking depth (>1 km) to the surface locking depth, within 4-6 m of the surface, above which slip is manifest as distributed surface shear. This barrier to surface slip is equated with a zone of phacoidal foliated gouge ubiquitous to the fault zone through Durmid Hill and the Mecca Hills. We speculate that internal rotation and translation of phacoidal clasts in this zone inhibits surface slip, transforming subsurface planar rupture into a zone of distributed surface shear. Deformation is distributed over a broad zone near the surface that in our current model takes the form of an arctangent function, whose fault-normal width is approximately six times its thickness.

Although the identification of a tough surface layer resistive to planar slip along the active trace of the San Andreas fault on Durmid Hill was unexpected, this rheology resembles that of Brooks et al., (2005) for the South Napa Fault. In order to account for the localized offset of channels, major earthquakes and large creep events in the Coachella Valley, must occasionally rupture through this surface shear zone. This has not occurred on Durmid Hill in the interval 2004-2020, but in 2017 may have occurred locally in the SE Mecca Hills (Tymovyeyeva et al., 2018).

Acknowledgements

This work was carried out at the Jet Propulsion Laboratory, California Institute of Technology, under a contract with the National Aeronautics and Space Administration (80NM0018D0004). Operation of the creepmeters was funded by USGS 2004 to 2011 and in 2019 by NSF EAR 1941558. Their data are archived at UNAVCO https://www.unavco.org/data/strain-seismic/creep-data/creep-data.html. Radar data for this research are available in the UAVSAR repository at the Alaska Satellite Facility, doi:10.5067/7PEQV8SVR4DM. © 2021. California Institute of Technology. Government sponsorship acknowledged.

References

Allen, C. R., M. Wyss, J. N. Brune, A. Granz, and R. Wallace (1972). Displacements on the Imperial, Superstition Hills, and San Andreas faults triggered by the Borrego Mountain

earthquake, in *The Borrego Mountain Earthquake, U.S. Geol, Surv. Profess. Paper 787*, 87-104.

Bilham, R., 2005. Coseismic strain and the transition to surface afterslip recorded by creepmeters near the 2004 Parkfield epicenter. *Seismological Research Letters*, *76*(1), pp.49-57.

Bilham, R. and Castillo, B., 2020. The July 2019 Ridgecrest, California, earthquake sequence recorded by creepmeters: Negligible epicentral afterslip and prolonged triggered slip at teleseismic distances. *Seismological Research Letters, 91(2A)*, pp.707-720.

Bilham, R. and Williams, P., 1985. Sawtooth segmentation and deformation processes on the southern San Andreas fault, California. *Geophysical Research Letters*, *12*(9), pp.557-560.

Brooks, B., Sarah E. Minson, Craig L. Glennie, Johanna M. Nevitt,Tim Dawson, Ron Rubin,Todd L. Ericksen, David Lockner, Kenneth Hudnut, Victoria Langenheim, Andrew Lutz, Maxime Mareschal, Jessica Murray, David Schwartz1 and Dana Zaccone (2017). Buried shallow fault slip from the South Napa earthquake revealed by near-field geodesy, *Science Advances 28 Jul 2017: 3, no. 7, e1700525* DOI: 10.1126/sciadv.1700525

Canny, J., 1986. A computational approach to edge detection. I*EEE Transactions on pattern analysis and machine intelligence, (6)*, pp.679-698.

Donnellan, A., Parker, J., Hensley, S., Pierce, M., Wang, J. and Rundle, J., 2014. UAVSAR observations of triggered slip on the Imperial, Superstition Hills, and East Elmore Ranch Faults associated with the 2010 M 7.2 El Mayor-Cucapah earthquake. *Geochemistry, Geophysics, Geosystems, 15(3)*, pp.815-829.

Donnellan, A., Grant Ludwig, L., Parker, J.W., Rundle, J.B., Wang, J., Pierce, M., Blewitt, G. and Hensley, S., 2015. Potential for a large earthquake near Los Angeles inferred from the 2014 La Habra earthquake. *Earth and Space Science, 2(9)*, pp.378-385.

Donnellan, A., Parker, J., Heflin, M., Lyzenga, G., Moore, A., Ludwig, L.G., Rundle, J., Wang, J. and Pierce, M., 2018. Fracture Advancing Step Tectonics Observed in the Yuha Desert and Ocotillo, CA, Following the 2010 Mw7. 2 El Mayor-Cucapah Earthquake. *Earth and Space Science, 5(9)*, pp.456-472.

Donnellan, A., Parker, J., Heflin, M, Glasscoe, M, Lyzenga, G, Pierce, M, Wang, J, Rundlt, J, Grant Ludwig, L, Granat, R, Mirkhanian, M, Pulver, N., 2021. Improving access to geodetic imaging crustal deformation data using GeoGateway. *Earth Science Informatics*. https://doi.org/10.1007/s12145-020-00561-7.

Grant, L. B**.** and A. Donnellan, 1855 and 1991 Surveys of the San Andreas Fault: Implications for Fault Mechanics, *Bulletin Seismological Society of America*, v. 84, no. 2, p.241-246, 1994.

Gray, H.J., Shobe, C.M., Hobley, D.E., Tucker, G.E., Duvall, A.R., Harbert, S.A. and Owen, L.A., 2018. Off-fault deformation rate along the southern San Andreas fault at Mecca Hills, southern California, inferred from landscape modeling of curved drainages. *Geology*, *46*(1), pp.59-62.

Heflin, M., Donnellan, A., Parker, J., Lyzenga, G., Moore, A., Ludwig, L.G., Rundle, J., Wang, J. and Pierce, M., 2020. Automated estimation and tools to extract positions, velocities, breaks, and seasonal terms from daily GNSS measurements: illuminating nonlinear Salton Trough deformation. *Earth and Space Science, 7(7)*, p.e2019EA000644.

Hensley, S., Wheeler, K., Sadowy, G., Jones, C., Shaffer, S., Zebker, H., Miller, T., Heavey, B., Chuang, E., Chao, R. and Vines, K., 2008, May. The UAVSAR instrument: Description and first results. In *2008 IEEE Radar Conference* (pp. 1-6). IEEE.

Hensley, S., Zebker, H., Jones, C., Michel, T., Muellerschoen, R. and Chapman, B., 2009, October. First deformation results using the NASA/JPL UAVSAR instrument. In *2009 2nd Asian-Pacific Conference on Synthetic Aperture Radar* (pp. 1051-1055). IEEE.

Jänecke, S.U., Markowski, D.K., Evans, J.P., Persaud, P. and Kenney, M., 2018. Durmid ladder structure and its implications for the nucleation sites of the next M> 7.5 earthquake on the San Andreas fault or Brawley seismic zone in southern California. *Lithosphere, 10(5)*, pp.602-631.

Jones, L.M., Bernknopf, R.L., Cox, D.A., Goltz, J., Hudnut, K.W., Mileti, D.S., Perry, S., Ponti, D.J., Porter, K.A., Reichle, M.S. and Seligson, H.A., 2008. *The ShakeOut Scenario: Effects of a potential M7.8 earthquake on the San Andreas fault in Southern California.* US Geological Survey.

Lindsey, E.O., Fialko, Y., Bock, Y., Sandwell, D.T. and Bilham, R., 2014. Localized and distributed creep along the southern San Andreas Fault. *Journal of Geophysical Research: Solid Earth, 119(10*), pp.7909-7922.

Lundgren, Paul, et al. "Southern San Andreas-San Jacinto fault system slip rates estimated from earthquake cycle models constrained by GPS and interferometric synthetic aperture radar observations." *Journal of Geophysical Research: Solid Earth 114.B2* (2009).

Parker, J., Glasscoe, M., Donnellan, A., Stough, T., Pierce, M. and Wang, J., 2018. Radar determination of fault slip and location in partially decorrelated images. In *Earthquakes and Multi-hazards Around the Pacific Rim, Vol. I* (pp. 101-116). Birkhäuser, Cham.

Philibosian, B., Fumal, T. and Weldon, R., 2011. San Andreas fault earthquake chronology and Lake Cahuilla history at Coachella, California. *Bulletin of the Seismological Society of America, 101(1)*, pp.13-38.

Rockwell, T.K., Meltzner, A.J. and Haaker, E.C., 2018. Dates of the Two Most Recent Surface Ruptures on the Southernmost San Andreas Fault Recalculated by Precise Dating of Lake Cahuilla Dry Periods, *Bulletin of the Seismological Society of America, 108(5A)*, pp.2634-2649.

Rymer, M.J., Treiman, J.A., Kendrick, K.J., Lienkaemper, J.J., Weldon, R.J., Bilham, R., Wei, M., Fielding, E.J., Hernandez, J.L., Olson, B.P. and Irvine, P.J., 2010. Triggered surface slips in southern California associated with the 2010 El Mayor-Cucapah, Baja California, Mexico, earthquake. *US Geological Survey Open-File Report, 1333*.

Savage, J.C. and Prescott, W.H., 1978. Asthenosphere readjustment and the earthquake cycle. *Journal of Geophysical Research: Solid Earth, 83(B7)*, pp.3369-3376.

Scott, C., Bunds, M., Shirzaei, M., & Toke, N. (2020). Creep along the Central San Andreas Fault from surface fractures, topographic differencing, and InSAR. Journal of Geophysical Research: Solid Earth, 125, e2020JB019762. https://doi.org/10.1029/2020JB019762

Sieh, K.E., 1986. Slip rate across the San Andreas fault and prehistoric earthquakes at Indio, California. *Eos Trans. AGU, 67(44)*, p.1200.

Sieh, K.E. and Williams, P.L., 1990. Behavior of the southernmost San Andreas fault during the past 300 years. *Journal of Geophysical Research: Solid Earth, 95(B5)*, pp.6629-6645.

Tymofyeyeva, E., Fialko, Y., Jiang, J., Xu, X., Sandwell, D., Bilham, R., Rockwell, T.K., Blanton, C., Burkett, F., Gontz, A. and Moafipoor, S., 2019. Slow Slip Event on the Southern San Andreas Fault Triggered by the 2017 M w 8.2 Chiapas (Mexico) Earthquake. *Journal of Geophysical Research: Solid Earth, 124(9)*, pp.9956-9975.

Tong, X., Smith-Konter, B. and Sandwell, D.T., 2014. Is there a discrepancy between geological and geodetic slip rates along the San Andreas Fault System? *Journal of Geophysical Research: Solid Earth, 119(3)*, pp.2518-2538.

Williams, P.L., McGill, S.F., Sieh, K.E., Allen, C.R. and Louie, J.N., 1988. Triggered slip along the San Andreas fault after the 8 July 1986 North Palm Springs earthquake. *Bulletin of the Seismological Society of America*, *78*(3), pp.1112-1122.

Xu, X., Ward, L.A., Jiang, J., Smith-Konter, B., Tymofyeyeva, E., Lindsey, E.O., Sylvester, A.G. and Sandwell, D.T., 2018. Surface creep rate of the southern San Andreas fault modulated by stress perturbations from nearby large events. *Geophysical Research Letters*, *45(19)*, pp.10-259.